

# HPMA-LMA Copolymer Drug Carriers in Oncology: An in Vivo PET Study to Assess the Tumor Line-Specific Polymer Uptake and Body Distribution

Mareli Allmeroth,<sup>†,§</sup> Dorothea Moderegger,<sup>‡,§</sup> Daniel Gündel,<sup>§</sup> Kaloian Koynov,<sup>||</sup> Hans-Georg Buchholz,<sup>⊥</sup> Kristin Mohr,<sup>#</sup> Frank Rösch,<sup>‡</sup> Rudolf Zentel,<sup>†</sup> and Oliver Thews<sup>\*,§</sup>

<sup>†</sup>Institute of Organic Chemistry, Johannes Gutenberg-University, Mainz, Germany

<sup>‡</sup>Institute of Nuclear Chemistry, Johannes Gutenberg-University, Mainz, Germany

<sup>§</sup>Institute of Physiology, University Halle, Halle (Saale), Germany

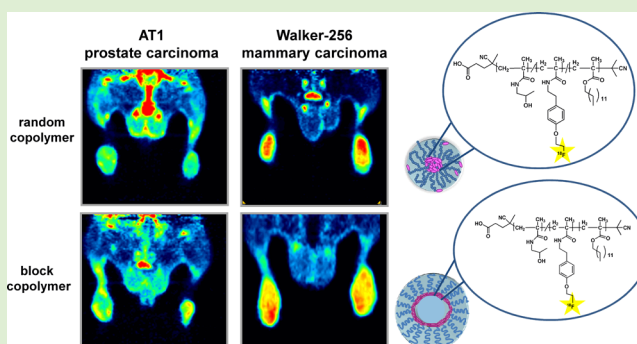
<sup>||</sup>Max-Planck-Institute for Polymer Research, Mainz, Germany

<sup>⊥</sup>Department of Nuclear Medicine, University Medicine Mainz, Germany

<sup>#</sup>Institute of Physical Chemistry, Johannes Gutenberg-University, Mainz, Germany

## S Supporting Information

**ABSTRACT:** Polymeric drug carriers aim to selectively target tumors in combination with protecting normal tissue. In this regard polymer structure and molecular weight are key factors considering organ distribution and tumor accumulation of the polymeric drug delivery system. Four different HPMA based copolymer structures (random as well as block copolymers with lauryl methacrylate as hydrophobic block) varying in molecular weight, size and resulting architecture were analyzed in two different tumor models (AT1 prostate carcinoma and Walker-256 mammary carcinoma) in vivo. Polymers were labeled with <sup>18</sup>F and organ/tumor uptake was followed by  $\mu$ PET imaging and *ex vivo* biodistribution. Vascular permeability was measured by dextran extravasation and vascular density by immunohistochemistry. Cellular polymer uptake was determined in vitro using fluorescence-labeled polymers. Most strikingly, the high molecular weight HPMA-LMA random copolymer demonstrated highest tumor uptake and blood pool concentration. The molecular structure (e.g., amphiphilicity) is holding a higher impact on desired in vivo properties than polymer size. The results also revealed pronounced differences between the tumor models although vascular permeability was almost comparable. Accumulation in Walker-256 carcinomas was much higher, presumably due to a better cellular uptake in this cell line and a denser vascular network in the tumors. These investigations clearly indicate that the properties of the individual tumor determine the suitability of polymeric drug carriers. The findings also illustrate the general necessity of a preclinical screening to analyze polymer uptake for each individual patient (e.g., by noninvasive PET imaging) in order to individualize polymer-based chemotherapy.



Polymer therapeutics<sup>1</sup> are a promising approach for anticancer treatment. The great benefit of polymer based drug delivery systems consists in a decrease of toxic side effects of the chemotherapeutic agent in healthy tissue, an accumulation in the tumor due to the enhanced permeability and retention (EPR) effect<sup>2</sup> and a longer blood circulation time compared to the pure anticancer drug. In this regard poly-*N*-(2-hydroxypropyl)methacrylamide poly(HPMA), being nontoxic, nonimmunogenic, and biocompatible, is holding favorable polymer characteristics for preclinical as well as clinical testing.<sup>3–7</sup> Such purely hydrophilic polymers interact, however, only moderately with the lipophilic cell membranes as a first step of drug uptake.

For this reason, several attempts have been undertaken to increase the lipophilicity of HPMA for instance by integrating lipids into the molecular structure.<sup>8</sup> Recently, it was suggested to use lauryl methacrylate (LMA) segments within the HPMA backbone to increase lipophilicity and by this improving the delivery of drugs over the blood-brain-barrier.<sup>9,10</sup> These HPMA-LMA-copolymers form self-assembled structures with a lipophilic core enabling the encapsulation of hydrophobic drug molecules and their subsequent release into the lipid cell membrane layer.

Received: May 17, 2013

Revised: August 1, 2013

Published: August 20, 2013

Due to the lipophilic segments these copolymers form superstructures (called aggregates or polymer micelles in the following) with hydrodynamic radii considerably larger than those of HPMA homopolymers. For this reason and based on the fact that lipophilic drugs can be dissolved in the hydrophobic core of these structures, HPMA-LMA copolymers are promising candidates for drug transport to tumors. However, the correlation between structural properties (e.g., molecular weight, aggregate size) of these copolymers and the ability of accumulating in tumors is still not fully understood. Besides molecular characteristics of the polymeric drug carrier also specific properties of the tumor could affect the tumor uptake. Cabral and co-workers<sup>11</sup> already demonstrated the effect of size of polymeric micelles on the uptake in poorly permeable tumor models. For instance, tumor vascularity and perfusion, vascular permeability, or metabolic parameters (such as oxygenation, pH or bioenergetic status) may affect the distribution and accumulation of nanotherapeutics.<sup>12</sup> Therefore, it is unclear whether the same polymer reaches comparable accumulation in different tumors.

Taking these considerations into account, the aim of the present study was to analyze different HPMA-LMA copolymer architectures concerning their biological distribution in vivo as a function of the tumor specific model. The polymer structures included random copolymers as well as block copolymers, both forming hydrophilic/hydrophobic superstructures and thus being interesting candidates for drug delivery.<sup>13–15</sup> However, before incorporating chemotherapeutic drugs into drug carriers, the aim of the present study is to analyze a functional structure–property relationship of the polymers. This analysis includes the identification of advantages and disadvantages of the differing molecular structures as well as the unimer/aggregate balance that may affect the body distribution, excretion through the kidneys, and accumulation in liver, spleen, and tumors. In order to test the impact of the individual tumor properties on the optimal drug carrier design all experiments were performed in two distinct tumor models (AT1 subline of the R-3327 Dunning prostate carcinoma and Walker 256 mammary carcinoma).

Besides ex vivo biodistribution, the body distribution and tumor accumulation was analyzed by noninvasive imaging using positron emission tomography (PET) allowing visualization of the pharmacokinetics in vivo, in real time and with high spatial resolution. Until now, studies concerning the in vivo behavior of diverse HPMA based formulations have been almost exclusively carried out using  $\gamma$ -imaging radionuclides, e.g., <sup>99m</sup>Tc or <sup>135</sup>I/<sup>131</sup>I,<sup>16,17</sup> which have a relatively low spatial resolution. Furthermore, there has been no systematic comparison between the pharmacokinetic profile of HPMA random and block copolymers in the literature so far. By radiolabeling the HPMA-LMA copolymers with the positron emitting isotope fluorine-18, the kinetics of tumor accumulation as well as whole body distribution of the polymers could be followed noninvasively at least for a time-interval of 4 h.<sup>18</sup>

## MATERIAL AND METHODS

**Materials.** All solvents were of analytical grade, as obtained by Sigma Aldrich and Acros Organics. Dioxane was distilled over a sodium/potassium composition. Lauryl methacrylate was distilled to remove the stabilizer and stored at  $-18^{\circ}\text{C}$ . 2,2'-Azo-bis(isobutyronitrile) (AIBN) was recrystallized from diethyl ether and stored at  $-18^{\circ}\text{C}$  as well.

**Polymer Synthesis.** The random and block HPMA-LMA-copolymers were synthesized according to the literature.<sup>13,18,19</sup> In brief, random copolymers were synthesized by reversible addition–fragmentation chain transfer (RAFT) polymerization of pentafluorophenyl methacrylate (PFMA) with lauryl methacrylate by help of 4-cyano-4-((thiobenzoyl) sulfanyl)pentanoic acid (CTP). As an example, 4 g of PFMA dissolved in 5 mL dioxane, lauryl methacrylate, AIBN, and CTP were mixed. The molar ratio of CTP/AIBN was chosen to be 8:1. After three freeze–vacuum–thaw cycles, the mixture was immersed in an oil bath at  $65^{\circ}\text{C}$  and stirred overnight. Afterward, poly(PFMA)-*ran*-poly(LMA) was precipitated three times in hexane, centrifuged, and dried under vacuum at  $40^{\circ}\text{C}$  overnight. A slightly pink powder was obtained. Yield: 54%. <sup>1</sup>H NMR (300 MHz, CDCl<sub>3</sub>)  $\delta$ / ppm: 0.84 (br t), 1.20–1.75 (br), 2.00–2.75 (br s). <sup>19</sup>F-NMR (400 MHz, CDCl<sub>3</sub>)  $\delta$ / ppm:  $-162.01$  (br),  $-156.95$  (br),  $-152$  to  $-150$  (br). The dithiobenzoate end group was removed using the protocol reported by Perrier et al.<sup>20</sup> Therefore, a 25-fold molar excess of AIBN was added to the polymer dissolved in dioxane. Afterward the polymer was precipitated in hexane and collected by centrifugation. The polymer was dried under vacuum. Yield: 75%. Removal of the dithioester end group could be proven by UV–vis spectroscopy.

For radioactive labeling of random copolymers, 100 mg of poly(PFMA)-*ran*-poly(LMA) copolymer was dissolved in 2 mL of absolute dioxane. As example, for the polymeric system P1\*, 5 mg of tyramine and 10 mg of triethylamine were diluted in a dimethyl sulfoxide (DMSO)/dioxane mixture and added to the vessel. After stirring for 4 h at  $35^{\circ}\text{C}$ , 30 mg of 1-aminopropan-2-ol as well as 40 mg of triethylamine were added, and the solution was stirred overnight. For final removal of reactive ester side groups, an additional 30 mg of 1-aminopropan-2-ol was added the next morning. The solution was precipitated two times in diethyl ether, centrifuged, and finally dissolved in a DMSO/water solution for dialysis. After lyophilization a white powder was obtained. Yield: 51%. <sup>1</sup>H NMR (400 MHz, d. DMSO)  $\delta$ / ppm: 0.70–0.90 (br), 0.90–1.40 (br), 1.40–1.90 (br), 2.75–3.10 (br), 3.50–3.80 (br), 4.50–4.75 (br), 6.60–6.75 (br), and 6.85–7.00 (br). For additional fluorescent labeling, 100 mg of polymeric precursor were diluted in 2 mL of absolute dioxane and 2.9 mg of Oregon Green 488 cadaverine were added. Afterward tyramine and 1-aminopropan-2-ol were added, as described above.

For synthesis of block copolymers, the macro-CTA obtained after homopolymerization of PFMA was dissolved in dioxane, afterward lauryl methacrylate and AIBN were added. The mixture was immersed in an oil bath at  $65^{\circ}\text{C}$  and stirred for 3 days. Afterward, poly(PFMA)-*b*-poly(LMA) was precipitated in ethanol, centrifuged, and dried under vacuum at  $40^{\circ}\text{C}$ . Yield: 54%. <sup>1</sup>H NMR (300 MHz, CDCl<sub>3</sub>)  $\delta$ / ppm: 0.84 (br t), 1.20–1.75 (br), 2.00–2.75 (br s). <sup>19</sup>F-NMR (400 MHz, CDCl<sub>3</sub>)  $\delta$ / ppm:  $-162.01$  (br),  $-156.95$  (br),  $-152$  to  $-150$  (br). For radioactive labeling as well as for fluorescent labeling, the above-mentioned synthetic route was applied. For more details, see the Supporting Information.

**Characterization.** <sup>1</sup>H NMR spectra were obtained by a Bruker AC 300 spectrometer at 300 MHz, <sup>19</sup>F-NMR analysis was carried out with a Bruker DRX-400 at 400 MHz. The synthesized polymers were dried under vacuum overnight, followed by gel permeation chromatography (GPC) in tetrahydrofuran (THF) as solvent. The flow rate was set to 1 mL/min with a temperature of  $25^{\circ}\text{C}$ .

Size exclusion chromatography (SEC) of <sup>18</sup>F-labeled polymers was performed using HiTrap Desalting Column, Sephadex G-25 Superfine with an UV-detector (2487  $\lambda$  absorbance detector) and a radio-detector.

The hydrodynamic radii of the polymeric systems were determined by fluorescence correlation spectroscopy using a commercial FCS setup (Zeiss, Germany) consisting of the module ConfoCor 2 and an inverted microscope. The fluorophores were excited with an argon laser ( $\lambda = 488$  nm), and the emission was collected after filtering with a LP505 long pass filter, and photon counting was performed with an avalanche photodiode. For sample preparation, stock solutions of 0.1 mg fluorescently labeled polymer/mL NaCl were used. A solution of free Oregon Green 488 cadaverine dye served as a control. The

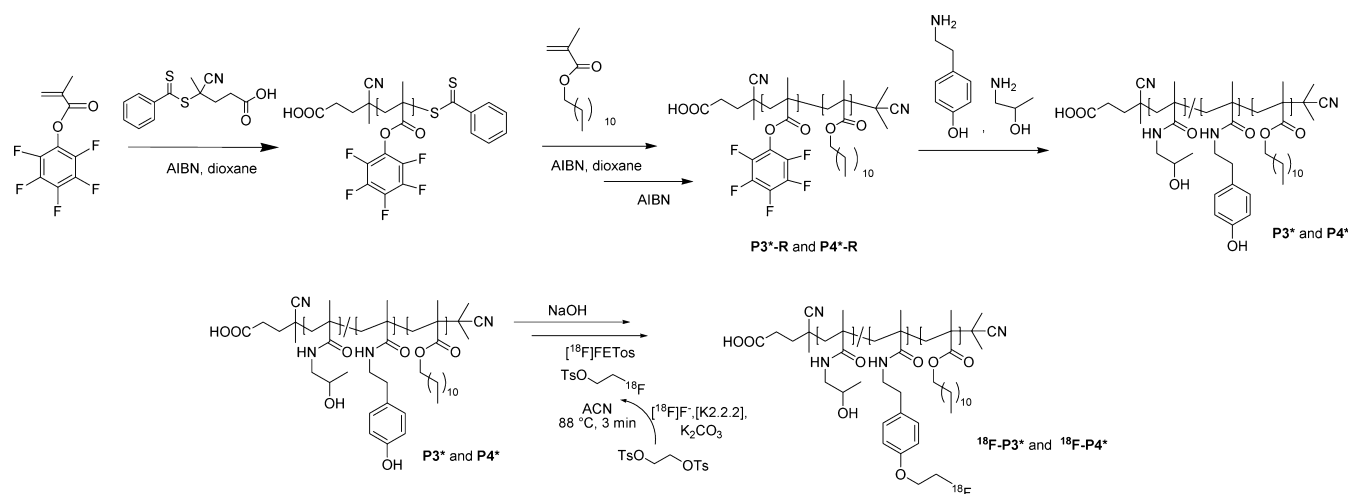


**Figure 1.** Reaction scheme of polymeric precursor systems (exemplary block copolymers with low (P3\*) and high (P4\*) molecular weight), their polymeranalogous conversion, and radioactive labeling procedure.

calibration of the FCS observation volume was performed using a dye with known diffusion coefficient, i.e., Rhodamine 6G. Time-dependent fluctuations of fluorescence intensity  $\delta I(t)$  were detected and evaluated by autocorrelation analysis, yielding the diffusion coefficient and hydrodynamic radius of the fluorescent species.<sup>21</sup> For more details, see the Supporting Information.

**Analysis of Aggregate Stability by Means of Dynamic Light Scattering (DLS).** The analysis of the aggregate stability was tested in human blood serum obtained from the University Clinic of Mainz. All solutions for light scattering experiments were prepared in a dust free flow box. Cylindrical quartz cuvettes (20 mm diameter, Hellma, Müllheim) were cleaned by dust-free distilled acetone, and serum solutions were filtered through Millex GS filters, 220 nm pore size (Millipore). Losses of serum proteins by filtration with Millex GS filters were negligible.<sup>22</sup> The high molecular weight random copolymer (P2\*) was prepared in isotonic sodium chloride solution (0.1 mg/mL). The polymer was filtered through an LCR450 nm filter into the light scattering cuvette. For the measurement of P2\* serum and polymer solution (dissolved in isotonic saline) were added into the light scattering cuvette resulting in a final concentration of 0.0625 mg polymer/mL in order to mimic in vivo conditions. The cuvette was incubated 20 min on a shaker at room temperature prior to the measurement. All light scattering experiments were accomplished with an instrument consisting of a HeNe laser (632.8 nm, 25 mW output power), an ALV-CGS 8F SLS/DLS 5022F goniometer equipped with eight simultaneously working ALV 7004 correlators and eight QEAPD Avalanche photodiode detectors. For more details, see the Supporting Information.

**Radioactive Labeling Procedure.** For  $^{18}\text{F}$ -labeling to an aqueous [ $^{18}\text{F}$ ]fluoride solution (2–8 GBq) Kryptofix 2.2.2., potassium carbonate and acetonitrile were added and the mixture was dried. To the residue ethyleneglycol-1,2-ditosylate in acetonitrile was added and heated under stirring. Purification was accomplished using HPLC and the collected fraction of 2-[ $^{18}\text{F}$ ]fluoroethyl-1-tosylate was diluted with water. The product was loaded on a Sep-Pak C18 cartridge, dried and eluted with DMSO.<sup>23</sup> The polymer precursor was dissolved in 200  $\mu\text{L}$  of dried DMSO and sodium hydroxide solution, and the previously eluted DMSO solution of 2-[ $^{18}\text{F}$ ]fluoroethyl-1-tosylate was added. After the labeling reaction, purification of the radiolabeled polymeric systems was accomplished by Sephadex G-25 size exclusion chromatography leading to a pure,  $^{18}\text{F}$ -labeled polymer solution ready for subsequent experiments.<sup>18,24</sup> For more details, see the Supporting Information.

**Tumor and Animal Models.** Information concerning cell lines (AT1 subline of the R-3327 Dunning prostate carcinoma and Walker 256 mammary carcinoma) and animal models are described in the Supporting Information. All experiments had previously been

approved by the regional animal ethics committee and were conducted in accordance with the German Law for Animal Protection and the UKCCCR Guidelines.<sup>25</sup>

#### Cellular Studies, Permeability Assay and Vascular Density.

The experimental setup is described in the Supporting Information.

#### In Vivo $\mu\text{PET}$ Imaging and Ex Vivo Biodistribution Studies.

Detailed information is given in the Supporting Information.

#### Autoradiographic Imaging and Histological Staining.

Details on the experimental setup are provided in the Supporting Information.

#### Statistical Analysis.

Results are expressed as means  $\pm$  SEM. Differences between groups were assessed by the two-tailed Wilcoxon test for unpaired samples and by multifactorial ANOVA. The significance level was set at  $\alpha = 5\%$  for all comparisons.

## RESULTS AND DISCUSSION

**Synthesis, Characterization and Radioactive Labeling of the HPMA Based Polymer Systems.** A library of HPMA based random and block copolymer structures was synthesized for analyzing their structure–property relationships in vivo. Starting from the reactive ester precursor pentafluorophenyl-methacrylate, reactive ester chemistry was combined with the controlled radical polymerization technique RAFT<sup>26,27</sup> for polymer preparation. This synthetic approach was intensively investigated in our laboratories in previous studies,<sup>19,28</sup> possessing the great benefit of creating narrowly distributed polymer precursor systems, which can be well-characterized by means of  $^1\text{H}$  NMR and GPC analysis. Further addition of lauryl methacrylate as hydrophobic block and AIBN as initiator is leading to PFPMA-*b*-LMA copolymer structures as seen in Figure 1. These precursor systems can then be easily converted to HPMA-based polymer structures via polymeranalogous reaction with 1-aminopropan-2-ol in a clean process. In this regard, the RAFT technique offers an elegant access to a variety of polymer architectures and functional groups. Molecular weight as well as hydrophobic content can be easily varied.<sup>13,18,24</sup> In combination with reactive ester chemistry, imaging moieties (e.g., fluorescent labeling) or therapeutics can be attached, enabling for example a successful in vivo or in vitro screening of the polymeric systems. Thus the incorporation of tyramine groups into the polymeric backbone via polymer-analogous reactions allowed us to use radioactive labeling ( $^{18}\text{F}$ ) for biodistribution studies in living animals (for reaction scheme, see Figure 1). Furthermore, with respect to the desired therapeutic application, an important advantage of the RAFT

**Table 1.** Analytical Data of Reactive Ester Random Copolymers (P1\*-R and P2\*-R) and Block Copolymers (P3\*-R and P4\*-R) As Well As the Final Polymers P1\* to P4\*<sup>a</sup>

nomenclature	polymeric structure	monomer ratio	$M_n$ in g/mol	$M_w$ in g/mol	PDI <sup>b</sup>	$R_h$ <sup>c</sup> in nm	cmc <sup>d</sup> in mg/mL
P1*-R	random copolymer	80:20% <sup>e</sup>	17000 <sup>b</sup>	21000 <sup>b</sup>	1.26	n.d.	-
P2*-R	random copolymer	80:20% <sup>e</sup>	57000 <sup>b</sup>	80000 <sup>b</sup>	1.41	n.d.	-
P3*-R	block copolymer	60:40% <sup>e</sup>	14000 <sup>b</sup>	18000 <sup>b</sup>	1.26	n.d.	-
P4*-R	block copolymer	60:40% <sup>e</sup>	25000 <sup>b</sup>	31000 <sup>b</sup>	1.25	n.d.	-
P1*	random copolymer	82:18 <sup>f</sup>	11000 <sup>g</sup>	14000 <sup>g</sup>	1.26	33.4	$4.6 \times 10^{-3}$
P2*	random copolymer	75:25 <sup>f</sup>	39000 <sup>g</sup>	55000 <sup>g</sup>	1.41	39.9	$1.6 \times 10^{-3}$
P3*	block copolymer	79:21 <sup>f</sup>	9000 <sup>g</sup>	12000 <sup>g</sup>	1.26	58.7	$5.6 \times 10^{-4}$
P4*	block copolymer	75:25 <sup>f</sup>	17000 <sup>g</sup>	21000 <sup>g</sup>	1.25	112.8	$2.1 \times 10^{-4}$

<sup>a</sup>Note that the diameter is twice the hydrodynamic radius  $R_h$ . <sup>b</sup>Determination by GPC in THF as solvent. <sup>c</sup>Hydrodynamic radii determined by fluorescence correlation spectroscopy (FCS) <sup>d</sup>As determined by surface tension versus concentration applying the ring method of the "du Noüy" ring tensiometer <sup>e</sup>Calculated ratio of PFPMA and LMA monomers within the polymer. <sup>f</sup>Monomer ratio determined by <sup>1</sup>H NMR spectroscopy after polymeranalogous reaction with 1-aminopropan-2-ol <sup>g</sup>Calculated from the molecular weights of the reactive ester polymers **random small-R** to **block large-R** as determined by GPC in THF as solvent.

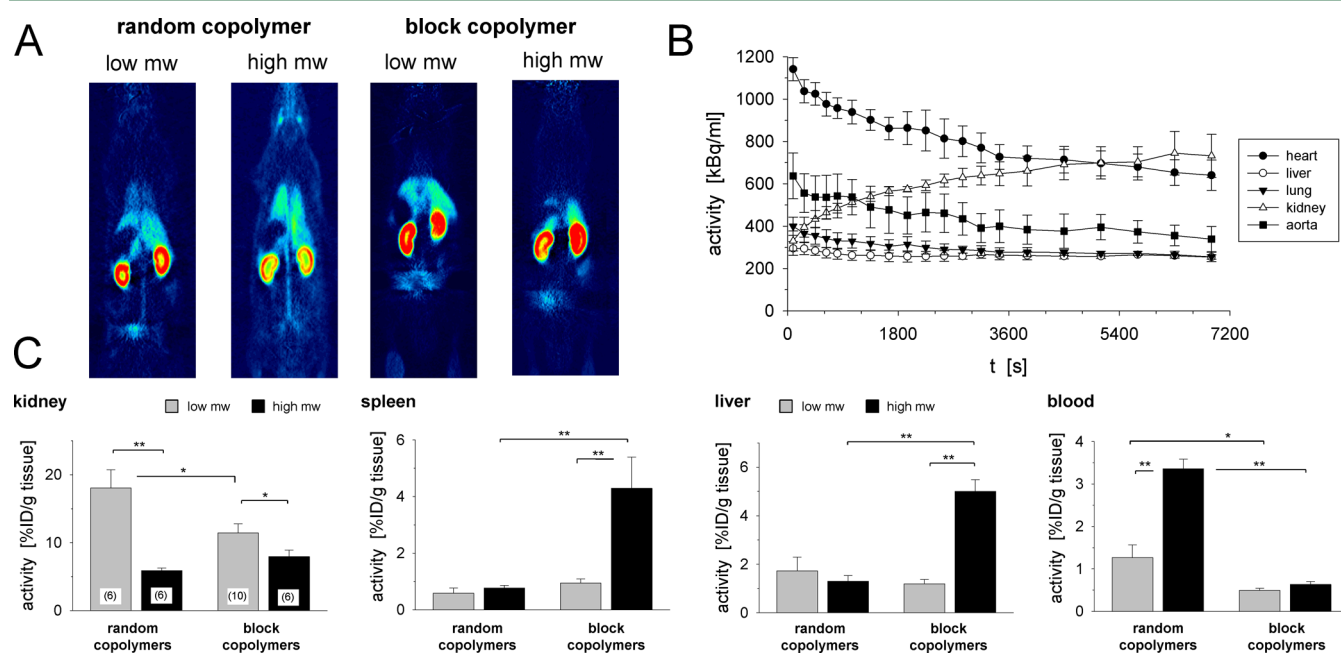


**Figure 2.** Organ distribution of the polymers (random and block copolymers with low or high molecular weight respectively). (A) Whole body PET images of the distribution of the polymers 2 h after polymer injection. (B) Time activity curves (TACs) for different organs after injection of the random copolymer with high molecular weight (P2\*);  $n = 2$ . (C) Quantification of the polymer uptake in different tissues. Uptake is expressed by the fraction of the injected dose (ID) of the polymer per gram tissue 2 h after i.v. injection.  $n = 5-10$ , (\*)  $p < 0.05$ , (\*\*)  $p < 0.01$ .

polymerization compared to the atom transfer radical polymerization (ATRP) is its high solvent and functionality tolerance as well as the absence of metal ions causing possible unwanted cytotoxicity. RAFT also benefits from the use of conventional radical initiators and low toxicity of some of the RAFT agents.<sup>29</sup>

As Table 1 shows, narrowly distributed (PDI 1.25–1.41) HPMA-based polymer architectures—random as well as block copolymers—could be synthesized, varying in molecular weight and hydrophobic content. The low molecular weight polymer structures (random copolymer P1\* and block copolymer P3\*) exhibited ~20% of lauryl methacrylate as the hydrophobic part; their high molecular weight counterparts (P2\* and P4\*) exhibited 25%. Table 1 also shows for the reactive ester polymers the “calculated monomer ratio” of HPMA and LMA monomers in the polymerization mixture. Surprisingly, the calculated monomer ratio in the feed differed from the actual incorporation efficacy within the final polymer. So far we do

not have a reasonable explanation for this discrepancy, and the phenomenon needs further investigation in future studies.

Due to this amphiphilic nature, the herein presented polymer structures form aggregates (polymer micelles) in water solutions (e.g., buffer). Thus the particle size can be varied between 60 and up to 220 nm in diameter thereby covering a wide spectrum of superstructures investigated in this study. Their molecular structure, the size of the aggregates (radius of the polymer micelles), as well as their critical micelle concentration (cmc) are summarized in Table 1.

The hydrodynamic radii of the nanosystems were measured by fluorescence correlation spectroscopy (FCS) using Oregon Green 488-labeled polymers. For the random copolymers (P1\*, P2\*), aggregate sizes of approximately 30 to 40 nm ( $R_h$ ) were determined, thus possessing almost comparable radii independent of the different molecular weight (14 kDa vs 55 kDa). For the block copolymers (P3\*, P4\*) hydrodynamic radii of 59 and 112 nm were detected. Stability of the aggregates in human

blood serum was exemplarily shown for the random copolymer with high  $M_w$  ( $P2^*$ ) by means of DLS. The aggregate size of  $\langle 1/R_h \rangle_{z-1} = 41$  nm was not affected by interaction with proteins from the serum. By means of DLS up to 24 h, no significant protein adsorption and aggregate formation with the polymers were detectable. Since previous studies<sup>18</sup> revealed a major impact of aggregate formation on the polymer biodistribution pattern for random copolymer particles, the herein presented polymer superstructures (HPMA-LMA random and block copolymers) were used to further investigate the influence of the molecular structure and particularly aggregate size on the pharmacokinetic profile in vivo. Even though the molecular weight of the single polymer chain (unimer) varied quite substantially between the molecules studied (Table 1), these molecules form aggregates with completely new biological properties and behavior. For instance, the polymer  $P2^*$  has a markedly higher molecular weight than  $P4^*$  but the hydrodynamic radius of the aggregate of  $P2^*$  is much smaller than  $P4^*$ . The aim of this study primarily focuses on the differences in aggregate sizes and polymer structures, having the predominant impact on the biodistribution in vivo.

The aggregates formed by our amphiphilic copolymers possess a complex inner structure. They are much too large ( $R_h = 30$ – $110$  nm) to be simple polymer micelles (inner hydrophobic core with a hydrophilic corona) because in this case they could not be much larger than the individual polymer chains (expected  $R_h$  about 2–6 nm). In comparison to what is known about random amphiphilic<sup>30,31</sup> and block copolymers,<sup>32</sup> the aggregates should consist of many small hydrophobic domains interconnected by a thin hydrophilic matrix. In addition the aggregates are in equilibrium with free polymer chains (unimers) like in micellar solutions. Judged from the cmc values (Table 1), which are a factor of 10 higher for the random copolymers, there are more free chains in equilibrium with the aggregates of random than of block copolymers.

In order to study the biodistribution and tumor accumulation of these nanosystems, the polymers were labeled with the positron emitting radionuclide  $^{18}\text{F}$ , which exhibits favorable nuclear characteristics ( $t_{1/2} = 110$  min, high  $\beta^+$ -branching, low beta energy) for high-resolution noninvasive PET imaging. Radiolabeling was accomplished in two steps using the prosthetic labeling synthon [ $^{18}\text{F}$ ]FETos, attached to the hydrophilic part of the polymer backbone by covalent linkage to tyramine groups (incorporation efficiency  $\sim 4\%$ ) (Figure 1).<sup>24</sup> Within each polymer architecture radiolabeling efficiencies were shown to be higher for polymers of lower molecular weight ( $P1^*$ ,  $P3^*$ ), which might result from the better accessibility of the tyramine groups. Following  $^{18}\text{F}$ -labeling, biodistribution of the labeled compounds was analyzed by  $\mu\text{PET}$  imaging as well as ex vivo organ concentration measurements in rats.

**Organ Distribution.** Using  $\mu\text{PET}$  imaging and ex vivo biodistribution analysis allows quantification of the polymer uptake in different organs. Figure 2A shows the whole body distribution pattern of the different polymers, Figure 2C demonstrates their quantitative pharmacokinetic profile in major organs (kidney, spleen, liver and blood) 2 h after i.v. injection. All polymers are renally cleared over the observed time frame. MicroPET imaging indicates predominant uptake in the kidneys, further increasing over time as shown in the time-activity curve (TAC) of the random copolymer with high  $M_w$  ( $P2^*$ ) (Figure 2B). The renal filtration of the different polymer structures could also be demonstrated by imaging the

bladder (Figure 2A) and by measuring the excretion in the urine. However, due to spontaneous urination during the observation period, the exact determination of the excreted amount of polymers was not feasible, and in some animals no urine could be collected. The amount of polymers found in the urine samples were  $7.0 \pm 2.8\%$  of the injected dose per gram urine for  $P1^*$ ,  $5.8 \pm 0.1\%$  for  $P2^*$ ,  $5.4 \pm 0.8\%$  for  $P3^*$  and  $0.9 \pm 0.5\%$  for  $P4^*$ , respectively. Taking the inconsistent collection of urine samples into account, these data indicate that all polymers were excreted by the kidney to a similar extent. Since all herein investigated polymer superstructures are too large (diameters between 60 and 220 nm) for glomerular filtration, the activity found in the urine could result from free polymer chains (unimers) which stay in an equilibrium with the superstructure aggregates and which could be filtered in the kidney glomerulus. Regarding the low molecular weight polymers ( $P1^*$ ,  $P3^*$ ) the unimers are so small that they can easily pass the kidney filter. When comparing only the polymers with low molecular weight ( $P1^*$ ,  $P3^*$ ), the block copolymer exhibits a lower cmc than the random copolymer. Taking this into account - together with the fact that block copolymers show a lower concentration of unimers compared to the random copolymer systems - the low  $M_w$  copolymer is excreted more slowly. This observation is in good agreement to already obtained results on low molecular weight HPMA based homopolymers (100% unimers), which are showing an even higher kidney uptake after 2 h p.i.<sup>18</sup> Considering the high molecular weight polymer structures ( $P2^*$  and  $P4^*$ ), there is an interference of unimer concentration and size. The random copolymer  $P2^*$ , exhibiting an  $R_h$  of 6 nm for single polymer chains, slowly accumulates in the kidney (Figure 2C) since its unimer size is already in the range of the renal threshold. In comparison, the block copolymer ( $P4^*$ ) is distinctly smaller (only half of the molecular weight), and although its critical micelle concentration is much lower, it is more efficiently renally cleared.

The second possibility for activity in the urine could be free  $^{18}\text{F}$  by degradation of the unimer. However, previous studies showed that radio-labeling of the HPMA-LMA-copolymers is stable in plasma,<sup>18</sup> leading to the conclusion that the activity found in the urine results from unimers reflecting the equilibrium between aggregates and single polymer chains. However, this assumption has to be proven in further measurements of the polymers in the urine.

Regarding liver uptake, a different pattern can be seen. All polymer structures—with exception of the high molecular weight block copolymer—accumulated poorly. In comparison, the liver concentration of large block copolymer ( $P4^*$ ) was 5-times higher than for all other polymers (Figure 2C, Supporting Information Table 1). This observation can be attributed to its big aggregate size of 220 nm in diameter. It is well-known from the literature that sizes in this range are triggering increased uptake by the mononuclear phagocyte system (MPS) and thus fast clearance from the blood pool.<sup>33,34</sup> After 4 h, the liver concentrations of the random copolymers were markedly, however, not statistically significant, lower (Supporting Figure 1), whereas for the block copolymers the concentration remained constant. In the biodistribution experiments, the spleen shows a similar uptake pattern as the liver (Figure 2C), with the high molecular weight block copolymer being taken up 4- to 5-times higher than all other polymers. In the spleen also phagocytosis by the MPS of the large particles may be responsible for the observed results.

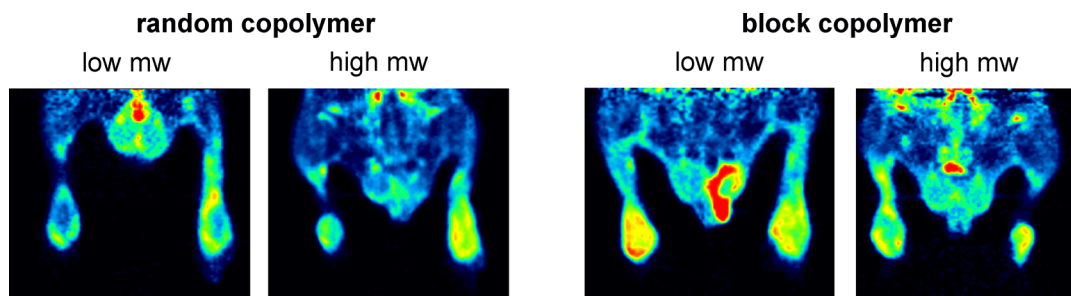


**Figure 3.** Comparison of the tumor uptake of the polymers (random and block copolymers with low or high molecular weight, respectively) in the same tumor model. Example PET images of polymer accumulation in AT1 tumors.

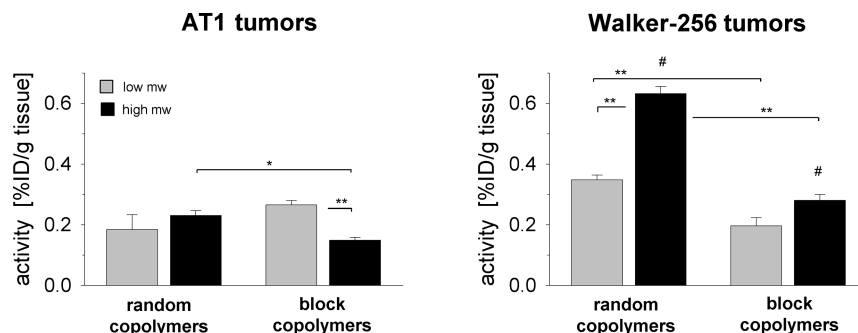


**Figure 4.** Intratumoral polymer concentration in AT1 prostate carcinomas and Walker-256 mammary carcinomas determined by biodistribution measurements 2 h after polymer application.  $n = 5-6$ ; (\*)  $p < 0.05$ , (\*\*)  $p < 0.01$ ; (#)  $p < 0.01$  Walker-256 vs AT1 tumors.

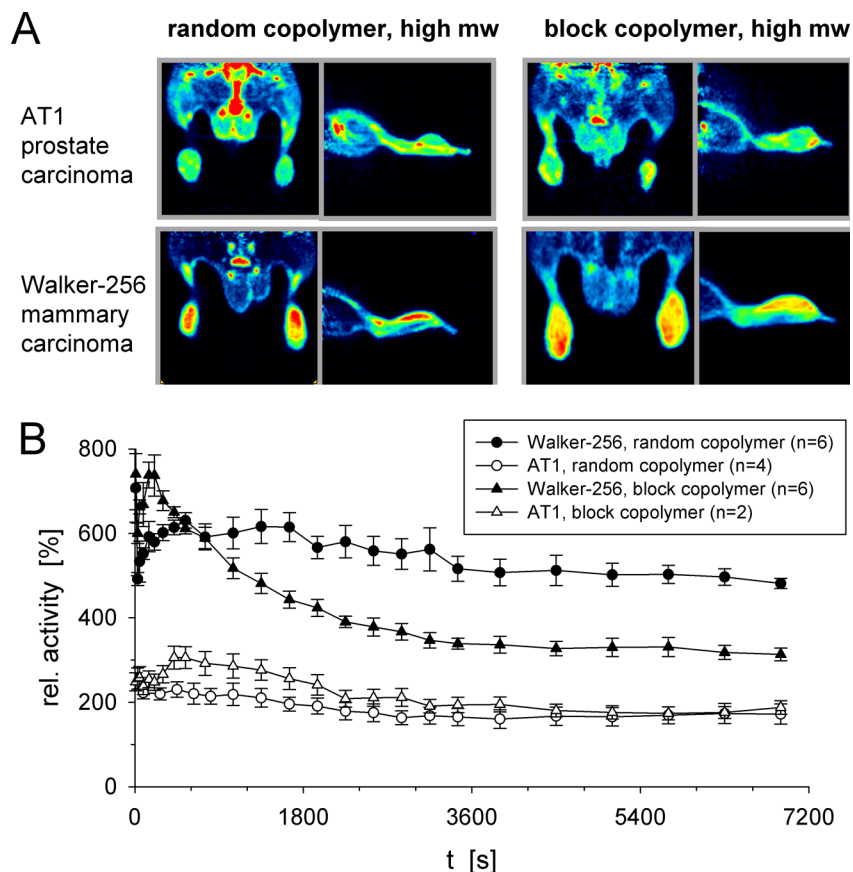


**Figure 5.** Comparison of uptake of the large random and block copolymers in two different tumor lines (AT1 and Walker-256 carcinomas). (A) Example PET images of the accumulation of the high molecular weight HPMA-*ran*-LMA and HPMA-*b*-LMA copolymer in AT1 and Walker-256 tumors. (B) Time course of the relative polymer uptake of the high  $M_w$  random (P2\*) and block (P4\*) copolymers in Walker-256 and AT1 tumors. Values were normalized to the concentration of the reference tissue (testis).

The blood values (Figure 2C) are directly reflecting the filtration processes. The blood level of the high molecular weight random copolymer ( $P2^*$ ) 2 and 4 h after injection was significantly higher (Supporting Figures 2 and 3) compared to the other polymer structures attributed to its specific polymer characteristics. Due to its high molecular weight  $P2^*$  is slowly filtered by the kidneys and its aggregate size of  $R_h$  around 40 nm is responsible for a low hepatic uptake.

The organ distribution in other tissues was not pronouncedly different among the studied polymer systems or the organ levels directly reflect the disparities in blood compartment (Supporting Table 1).

**Tumor Accumulation.** The major aim of the presented study was to analyze the polymer uptake in two different tumor models (AT1 prostate carcinoma, Walker-256 mammary carcinoma of the rat) applying PET as a fast and versatile imaging tool. Both tumor cell lines were implanted subcutaneously into the hind foot dorsum and grew with a comparable rate, 7 to 14 days to reach a mean volume of  $1.32 \pm 0.10$  mL. Even though both tumor models show similar growth rate and comparable histology, the uptake of the polymers was fundamentally different. Figure 3 shows the uptake of all four polymers in AT1 prostate carcinomas. All polymers accumulated poorly in this tumor model, and the uptake was almost unaffected by the molecular structure and/or aggregate size (Figures 3 and 4). Neither polymeric structure ( $p = 0.927$  ANOVA) nor molecular weight ( $p = 0.207$ ) had a relevant impact on intratumoral concentrations, although the blood levels were varying noticeably between the different polymer architectures (especially for the random copolymers ( $P1^*$ ,  $P2^*$ ), Figure 2C). When analyzing the spatial distribution of the intratumoral uptake in AT1 tumors, PET imaging revealed that the highest concentrations were found in the outer rim of AT1 tumors, a phenomenon seen more or less with all polymers (Figure 3). For more detailed evaluation of the spatial heterogeneity, autoradiograms were generated and correlated with the histological structure. These microscopic images illustrated that the high concentration in the rim corresponds to the subcutis around the tumor and not to the tumor tissue itself (Figure 6A). Since the *ex vivo* biodistribution studies were performed in tumor tissue without skin, the values shown in Figure 4 are not biased by the subcutaneous blood compartment.

In the PET images which show the maximum intensity projection of the field of view, one might have the impression that there is also a noticeable polymer uptake in normal tissues (e.g., skeletal muscle of the hind leg). However, the 3D analysis of the tissue reveals that the polymer is located only intravascular. It has also to be taken into account that the raw PET images (Figures 3 and 5A) show only relative values since the color-coding cannot be calibrated. In the panel for the low  $M_w$  block copolymer shown in Figure 3 a strong accumulation of activity was found close to the testes. However, this activity was not inside the body but a result of spontaneous urination of the animal.

In Walker-256 tumors the uptake was markedly different, depending on the polymer architecture as well as the molecular weight. Whereas the block copolymers were accumulated poorly in the Walker tumors (comparable to AT1 tumors), the uptake of the HPMa-*ran*-LMA copolymers was significantly higher (Figures 4 and 5). The intratumoral concentration of the large random copolymer ( $P2^*$ ) was 2.2-times higher than for the large block copolymer ( $P4^*$ ) and almost 3-times higher

than the HPMa-*ran*-LMA copolymer levels in AT1 tumors (Figures 4+5). Since the random copolymer particles stay much longer in the circulation (blood pool, Figure 2C) one possible explanation could be the difference of vascularity of AT1 and Walker-256 carcinoma. But also differences in vascular leakiness or the cellular uptake of the polymers could be responsible for this finding.

The low molecular weight random copolymer ( $P1^*$ ) also showed a markedly (however, not statistically significant  $p = 0.055$ ) higher concentration in Walker carcinomas as compared to AT1 tumors. The absolute level of low  $M_w$  random copolymer ( $P1^*$ ), however, was lower than for high  $M_w$  counterpart ( $P2^*$ ) (Figure 4), which might be the result of a lower blood concentration of  $P1^*$  (Figure 2C). Besides others, one possible explanation might be the lower hydrophobicity of the small random copolymer (incorporation efficiency of 18% LMA) compared to its high molecular weight counterpart (25% of LMA-fraction). The uptake of the random copolymers depend mainly on the tumor entity (Figure 5A+B) which was confirmed by ANOVA ( $p < 0.0001$ ). The uptake of the block copolymers was much lower than for the random copolymer structures. These data clearly reveal that the intratumoral uptake of polymers is not only a question of molecular size<sup>11</sup> (which was highest for the block copolymers, Table 1) but also strongly dependent on the chemical properties of the polymer architectures (e.g., hydrophobicity/hydrophilicity). However, for a distinct polymeric structure the differences between the tumor lines are tremendous (at least for the random copolymers) indicating that specific tumor cell properties also strongly affect intratumoral polymer accumulation.

Analyzing the kinetics of polymer uptake in both tumor lines by PET imaging revealed that stable intratumoral concentrations were reached 15–20 min after injection, however, with differences depending on the polymer structure (Figure 5B). After rapid redistribution processes during the first minutes after polymer injection, the concentration of the large random copolymer ( $P2^*$ ) remained almost stable over the period of 2 h, whereas the concentration of the large block copolymer ( $P4^*$ ) decreased markedly during the observation period (in Walker-256 tumors more pronouncedly than in AT1 tumors). These results indicate that the block copolymers stay preferentially in the blood compartment and the tumor concentration decreases with the reduction of the blood level. However, the random copolymers seem to extravasate more effectively, accumulate in the tumor tissue, and stay there although the blood concentration decreases. These data indicate that tumor accumulation is affected by either the vascular permeability in the tumor tissue but also by the retention time of the polymer in the circulation.

When comparing the polymers with respect to their molecular weight, the biodistribution data reveal that the concentration in Walker-256 tumors of both high molecular weight copolymers ( $P2^*$ ,  $P4^*$ ) remained constantly on a higher level - even over a longer time span up to 4 h (Supporting Figure 3) although the blood concentration was markedly decreasing over time (Supporting Figure 1). The tumor concentration of the low molecular weight polymers ( $P1^*$ ,  $P3^*$ ) decreased markedly. These data indicate that high  $M_w$  polymers were retained in the tumor tissue, whereas the small polymers were washed out.

From the results on tumor uptake the question arises why the HPMa-*ran*-LMA copolymers accumulated differently in both tumor models. Three tumor specific factors might be of

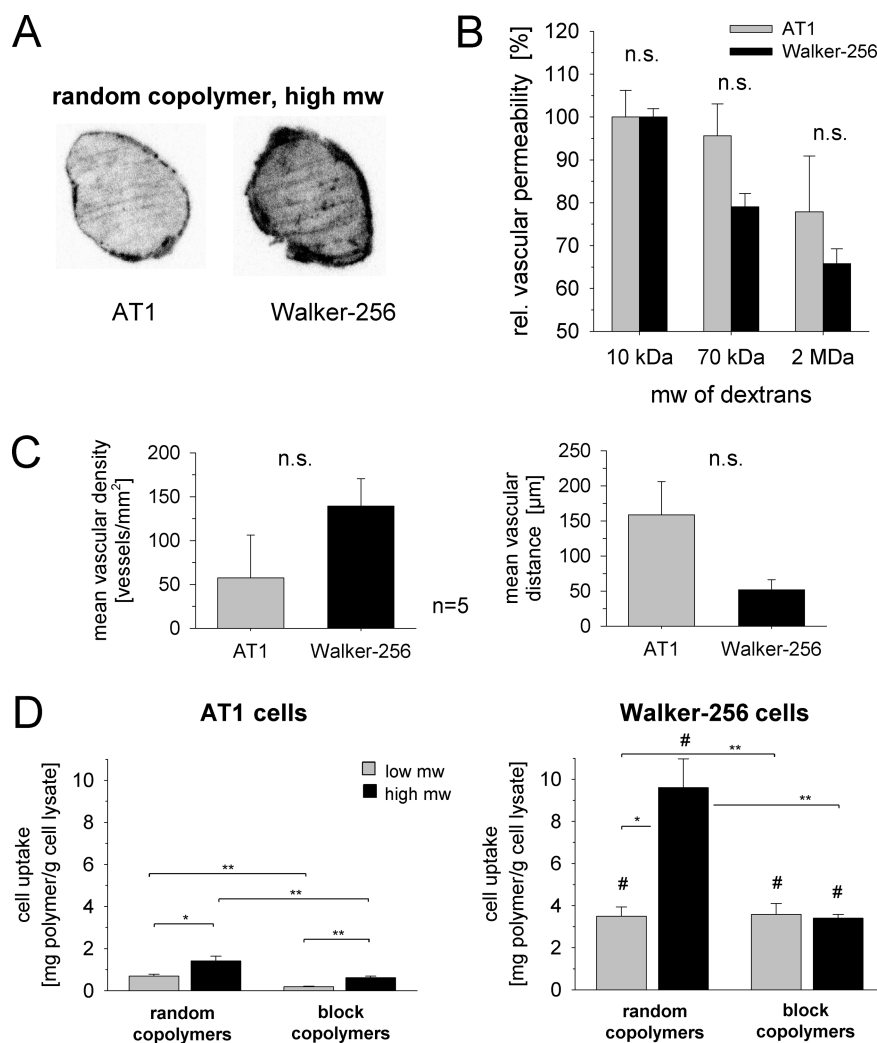


**Figure 6.** Differences of intratumoral uptake distribution. (A) Autoradiographic images of the polymer distribution within the tumor. (B) Vascular permeability of AT1 and Walker-256 tumors in vivo measured by extravasation of dextrans of different molecular weights ( $M_w$ ).  $n = 2-6$ . (C) Vascular density and average distance to the next neighboring blood vessels in AT1 and Walker-256 tumors. (D) Cellular uptake of the polymers after 2 h incubation at 37 °C in AT1 and Walker-256 carcinoma cells in vitro;  $n = 6-12$ , (\*)  $p < 0.05$ , (\*\*)  $p < 0.01$ . (#)  $p < 0.01$  Walker-256 vs AT1 cells.

importance: (1) differences in vascular density, (2) differences in vascular permeability and (3) differences in cellular uptake of the polymer.

Since previous studies of Cabral and co-workers demonstrated that vascular permeability affects the tumor uptake of nanosized structures,<sup>11</sup> this parameter was measured in the tumor models used in the present study by determining the extravasation of dextrans with different molecular weights (10, 70, 2000 kDa). The hydrodynamic radii of the fluorescence labeled dextrans were  $1.8 \pm 0.1$  nm,  $14.4 \pm 1.0$  nm and  $35.0 \pm 2.2$  nm, respectively. Especially the 2000 kDa dextran showed a radius comparable to those of the HPMA-*ran*-LMA copolymers (Table 1). As shown in Figure 6B, the vascular permeability for high molecular weight dextrans was slightly (but not statistically significant) different between the two tumor lines. However, although AT1 tumors showed a much lower uptake of the HPMA-*ran*-LMA copolymers compared to Walker-256 tumors, the vascular permeability of these tumors was found to be even higher (Figure 6B). Studies by other groups have analyzed the vascular permeability of either AT1 or Walker-256 tumors and showed that both tumors were moderately permeable for

molecules up to a molecular weight of approximately 50–60 kDa, but they seem to be more or less impermeable for molecules over 90 kDa.<sup>35,36</sup> Nonetheless, the results of these studies are difficult to compare with each other due to different techniques used for measuring vascular permeability, whereas the results of the present study (as shown in Figure 6B) used the same experimental procedure under identical conditions. In the previous studies an equilibrium between blood pool and interstitial space for molecules up to 50–60 kDa was reached at least 60 min post injection.<sup>36</sup> The concentrations of the polymer used in the present study also reached a stable value within 2 h (even for the block copolymer which exhibits a markedly lower molecular weight but has the ability to form regular micellar structures). Especially for the large polymers the tumor concentration remained stable over the whole observation period (up to 4 h; Supporting Figure 3) in both tumor models.

The results concerning the HPMA-*ran*-LMA copolymers, however, are somehow surprising. In contrast to the block copolymers, these nanoparticles were markedly accumulated in Walker-256 tumors but not in AT1 tumors (although the

vascular permeability was lower in Walker-256 tumors, Figure 6B). Beyond that, the high molecular weight random copolymer ( $M_n = 39$  kDa) was taken up much stronger than its low molecular weight counterpart ( $M_n = 11$  kDa). Therefore other mechanisms besides vascular permeability have to be considered. Analysis of the vascular network in both tumor lines revealed a higher (however, due to pronounced intertumoral heterogeneity not statistically significant) vascular density with shorter intervessel distance in Walker-256 tumors compared to AT1 tumors (Figure 6C). For this reason, the higher concentration found in the Walker-256 tumors by PET imaging might be at least partially the result of a larger blood vessel compartment in these tumors. However, the vessel density alone cannot explain the observed differences since the concentration of the block copolymers were not different between the two tumor models (Figure 4).

In a further in vitro experiment, the cellular uptake of the polymers into AT1 and Walker-256 cells was measured. The cell uptake depended significantly on the tumor cell line ( $p = 0.0001$ , ANOVA). As shown in Figure 6D, all polymers were taken up in AT1 cells to only a very small extent. However, the uptake of the HPMA-*ran*-LMA copolymers in Walker-256 cells was approximately 4–6 times higher than in AT1 (Figure 6D). These tumor cells exhibit distinct features leading to a much better cellular uptake, which might explain the differences in the ex vivo biodistribution experiments. Although differences in the endocytic processes of both lines might explain these findings, the reason for this differential behavior presently still remains unclear. The cellular uptake pattern (Figure 6D) was similar to the whole tumor tissue results (Figure 4), indicating that the combination of in vivo and in vitro experiments constitutes a beneficial platform for determining the suitability of polymers as drug carrier systems.

The results presented describe a structure–property relationship of diverse polymer architectures that exhibit different sizes and superstructures influencing their biodistribution as well as tumor accumulation. In the next step, these polymeric structures need to be combined with a therapeutic drugs to proof the advantages of the whole system. However, the previous analysis of the impact of polymer design on subsequent biodistribution is necessary to distinguish between the effects of quality/efficiency of drug delivery to the tumor tissue and cytotoxic efficacy in the cell (which depends on numerous other factors, e.g., route of cellular incorporation or stability of the polymer-drug binding and drug release).

## CONCLUSION

The present study clearly demonstrates that polymer architecture, the resulting aggregate formation, as well as the size of the unimers (existing in equilibrium) affect the body distribution of HPMA based polymers. Using radiolabeling of the polymers with positron emitting isotopes ( $^{18}\text{F}$ ) allows biodistribution analysis as well as noninvasive PET-imaging for quantification purposes. The study clearly illustrates that numerous factors are responsible for determining the intratumoral accumulation and body distribution of HPMA-LMA-copolymers:

1. Molecular weight of the polymers: When comparing the same polymeric structure (random or block copolymer) with differing molecular weight (low  $M_w$  vs high  $M_w$ ), the aggregates of the high molecular weight polymers stayed

longer in circulation and showed a better tumor accumulation in Walker 256 carcinomas.

2. Size of the polymer aggregates: The organ distribution and tumor accumulation is strongly dependent on the kind of aggregate formed, which becomes most obvious when comparing the high  $M_w$  random and block copolymer ( $\text{P2}^*$  and  $\text{P4}^*$ ). Surprisingly, the aggregates with smaller hydrodynamic radius ( $\text{P2}^*$ ) stayed longer in the blood compartment and were better accumulated in the tumor. Besides the aggregate size, lipophilicity of the aggregate might play a role.
3. Tumor model: The two tumor models used in the present study showed profound differences in polymer uptake although the proliferation rate or histological characteristics were comparable. Differences in the size of the vascular compartments in both tumor models could be at least partially responsible for it. However, the cell experiments clearly reveal that the cellular uptake of the polymers varies markedly between the two cell lines used and could explain (at least to a certain degree) the differences seen in vivo.

The results also demonstrate that the efficacy of a tumor treatment by polymer drug nanocarriers depends strongly on the properties of each individual tumor. The ideal polymer for nanocarrier chemotherapy has to be chosen for individual tumors. Concerning the clinical setting, the present studies underline the necessity of a precise polymer characterization in combination with its preclinical screening to tailor the polymer carrier system for each individual tumor and patient to be treated. In this regard radiolabeling combined with imaging of the polymer distribution in vivo seems to be a promising analytical tool for the individualization of polymer-based chemotherapy.

## ASSOCIATED CONTENT

### Supporting Information

(A) Material and Methods: Detailed description of the experimental procedures. (B) Figure 1: Comparison of the organ distribution. (C) Figure 2: PET image of the body distribution of the high molecular weight random copolymer ( $\text{P2}^*$ ) averaged over the time interval from 15' and 120' post polymer injection. (D) Figure 3: Intratumoral concentration of polymers. (E) Table 1: Polymer uptake in different organs. This material is available free of charge via the Internet at <http://pubs.acs.org>.

## AUTHOR INFORMATION

### Corresponding Author

\*Address: Institute of Physiology Martin-Luther-University Halle, Magdeburger Strasse 6, 06112 Halle (Saale), Germany. Phone: +49-0345-557 4048. Fax: +49-0345-557 4019. E-mail: [oliver.thews@medizin.uni-halle.de](mailto:oliver.thews@medizin.uni-halle.de).

### Author Contributions

<sup>§</sup>both authors contributed equally

### Notes

The authors declare no competing financial interest.

## ACKNOWLEDGMENTS

The authors would like to thank Barbara Biesalski, Nicole Bausbacher, and Bengü Yilmaz for their support during animal studies and following interpretation as well as Prof. Dr. Faramarz Dehghani for valuable assistance for immunohisto-

chemistry. We also want to thank the Max-Planck Graduate Center (MPGC, M. Allmeroth) as well as the Graduate School Materials Science in Mainz (Excellence Initiative, DFG/GSC 266, D. Moderegger) for financial support. In addition, the authors are very thankful for financial support of the DFG (Rösch: RO 985/30-1; Thews: TH 482/4-1, Zentel: ZE 230/21-1) and SAMT Initiative Mainz. Furthermore, thanks to Dr. Matthias Barz and Prof. Dr. Manfred Schmidt for fruitful discussion.

## REFERENCES

- (1) Duncan, R. The dawning era of polymer therapeutics. *Nat. Rev. Drug Discovery* **2003**, *2*, 347–360.
- (2) Matsumura, Y.; Maeda, H. A new concept for macromolecular therapeutics in cancer chemotherapy: Mechanism of tumoritropic accumulation of proteins and the antitumor agent smancs. *Cancer Res.* **1986**, *46*, 6387–6392.
- (3) Duncan, R. Development of HPMA copolymer-anticancer conjugates: Clinical experience and lessons learnt. *Adv. Drug Deliv. Rev.* **2009**, *61*, 1131–1148.
- (4) Lammers, T. Improving the efficacy of combined modality anticancer therapy using HPMA copolymer-based nanomedicine formulations. *Adv. Drug Deliv. Rev.* **2010**, *62*, 203–230.
- (5) Minko, T.; Kopecková, P.; Pozharov, V.; Kopecek, J. HPMA copolymer bound adriamycin overcomes MDR1 gene encoded resistance in a human ovarian carcinoma cell line. *J. Controlled Release* **1998**, *54*, 223–233.
- (6) Nowotnik, D. P.; Cvitkovic, E. ProLinda(TM) (AP5346): A review of the development of an HPMA DACH platinum Polymer Therapeutic. *Adv. Drug Deliv. Rev.* **2009**, *61*, 1214–1219.
- (7) Ulbrich, K.; Subr, V. Structural and chemical aspects of HPMA copolymers as drug carriers. *Adv. Drug Deliv. Rev.* **2010**, *62*, 150–166.
- (8) Filippov, S. K.; Chytil, P.; Konarev, P. V.; Dyakonova, M.; Papadakis, C.; Zhigunov, A.; Plestil, J.; Stepanek, P.; Etrych, T.; Ulbrich, K.; Svergun, D. I. Macromolecular HPMA-based nanoparticles with cholesterol for solid-tumor targeting: Detailed study of the inner structure of a highly efficient drug delivery system. *Biomacromolecules* **2012**, *13*, 2594–2604.
- (9) Hemmelmann, M.; Knoth, C.; Schmitt, U.; Allmeroth, M.; Moderegger, D.; Barz, M.; Koynov, K.; Hiemke, C.; Rosch, F.; Zentel, R. HPMA based amphiphilic copolymers mediate central nervous effects of domperidone. *Macromol. Rapid Commun.* **2011**, *32*, 712–717.
- (10) Hemmelmann, M.; Metz, V. V.; Koynov, K.; Blank, K.; Postina, R.; Zentel, R. Amphiphilic HPMA-LMA copolymers increase the transport of Rhodamine 123 across a BBB model without harming its barrier integrity. *J. Controlled Release* **2012**, *163*, 170–177.
- (11) Cabral, H.; Matsumoto, Y.; Mizuno, K.; Chen, Q.; Murakami, M.; Kimura, M.; Terada, Y.; Kano, M. R.; Miyazono, K.; Uesaka, M.; Nishiyama, N.; Kataoka, K. Accumulation of sub-100 nm polymeric micelles in poorly permeable tumours depends on size. *Nat. Nanotechnol.* **2011**, *6*, 815–823.
- (12) Heuser, L. S.; Miller, F. N. Differential macromolecular leakage from the vasculature of tumors. *Cancer* **1986**, *57*, 461–464.
- (13) Barz, M.; Luxenhofer, R.; Zentel, R.; Kabanov, A. V. The uptake of *N*-(2-hydroxypropyl)-methacrylamide based homo, random and block copolymers by human multi-drug resistant breast adenocarcinoma cells. *Biomaterials* **2009**, *30*, 5682–5690.
- (14) Kataoka, K.; Harada, A.; Nagasaki, Y. Block copolymer micelles for drug delivery: Design, characterization and biological significance. *Adv. Drug Deliv. Rev.* **2001**, *47*, 113–131.
- (15) Talelli, M.; Rijcken, C. J. F.; van Nostrum, C. F.; Storm, G.; Hennink, W. E. Micelles based on HPMA copolymers. *Adv. Drug Deliv. Rev.* **2010**, *62*, 231–239.
- (16) Kissel, M.; Peschke, P.; Subr, V.; Ulbrich, K.; Strunz, A.; Kühnlein, R.; Debus, J.; Friedrich, E. Detection and cellular localisation of the synthetic soluble macromolecular drug carrier pHPMA. *Eur. J. Nucl. Med. Mol. Imaging* **2002**, *29*, 1055–1062.
- (17) Lu, Z. R. Molecular imaging of HPMA copolymers: Visualizing drug delivery in cell, mouse and man. *Adv. Drug Deliv. Rev.* **2010**, *62*, 246–257.
- (18) Allmeroth, M.; Moderegger, D.; Biesalski, B.; Koynov, K.; Rösch, F.; Thews, O.; Zentel, R. Modifying the body distribution of HPMA-based copolymers by molecular weight and aggregate formation. *Biomacromolecules* **2011**, *12*, 2841–2849.
- (19) Theato, P. Synthesis of well-defined polymeric activated esters. *J. Polymer Sci. Part A: Polymer Chem.* **2008**, *46*, 6677–6687.
- (20) Perrier, S.; Takolpuckdee, P.; Mars, C. A. Reversible addition-fragmentation chain transfer polymerization: End group modification for functionalized polymers and chain transfer agent recovery. *Macromolecules* **2005**, *38*, 2033–2036.
- (21) Rigler, R.; Elson, E. S. *Fluorescence Correlation Spectroscopy: Theory and Applications*; Springer: Heidelberg, Germany, 2001.
- (22) Rausch, K.; Reuter, A.; Fischer, K.; Schmidt, M. Evaluation of Nanoparticle Aggregation in Human Blood Serum. *Biomacromolecules* **2010**, *11*, 2836–2839.
- (23) Bauman, A.; Piel, M.; Schirmacher, R.; Rösch, F. Efficient alkali iodide promoted <sup>18</sup>F-fluoroethylations with 2-[<sup>18</sup>F]fluoroethyl tosylate and 1-bromo-2-[<sup>18</sup>F]fluoroethane. *Tetrahedron Lett.* **2003**, *44*, 9165–9167.
- (24) Herth, M. M.; Barz, M.; Moderegger, D.; Allmeroth, M.; Jahn, M.; Thews, O.; Zentel, R.; Rösch, F. Radioactive labeling of defined HPMA-based polymeric structures using [<sup>18</sup>F]FETos for in vivo imaging by positron emission tomography. *Biomacromolecules* **2009**, *10*, 1697–1703.
- (25) Workman, P.; Aboagye, E. O.; Balkwill, F.; Balmain, A.; Bruder, G.; Chaplin, D. J.; Double, J. A.; Everitt, J.; Farningham, D. A.; Glennie, M. J.; Kelland, L. R.; Robinson, V.; Stratford, I. J.; Tozer, G. M.; Watson, S.; Wedge, S. R.; Eccles, S. A. Guidelines for the welfare and use of animals in cancer research. *Br. J. Cancer* **2010**, *102*, 1555–1577.
- (26) Chiefari, J.; Chong, Y. K.; Ercole, F.; Krstina, J.; Jeffery, J.; Le, T. P. T.; Mayadunne, R. T. A.; Meijs, G. F.; Moad, C. L.; Moad, G.; Rizzardo, E.; Thang, S. H. Living free-radical polymerization by reversible addition-fragmentation chain transfer: The RAFT process. *Macromolecules* **1998**, *31*, 5559–5562.
- (27) Moad, G.; Rizzardo, E.; Thang, S. H. Living radical polymerization by the RAFT process. *Aust. J. Chem.* **2005**, *58*, 379–410.
- (28) Eberhardt, M.; Mruk, R.; Zentel, R.; Théato, P. Synthesis of pentafluorophenyl(meth)acrylate polymers: New precursor polymers for the synthesis of multifunctional materials. *Eur. Polym. J.* **2005**, *41*, 1569–1575.
- (29) Boyer, C.; Bulmus, V.; Davis, T. P.; Ladmiral, V.; Liu, J.; Perrier, S. b. Bioapplications of RAFT polymerization. *Chem. Rev.* **2009**, *109*, 5402–5436.
- (30) Hemmelmann, M.; Kurzbach, D.; Koynov, K.; Hinderberger, D.; Zentel, R. Aggregation behavior of amphiphilic p(HPMA)-co-p(LMA) copolymers studied by FCS and EPR spectroscopy. *Biomacromolecules* **2012**, *13*, 4065–4074.
- (31) Laschewsky, A. Molecular concepts, self-organisation and properties of polysoaps. *Adv. Polym. Sci.* **1995**, *124*, 1–86.
- (32) Yu, K.; Eisenberg, A. Bilayer morphologies of self-assembled crew-cut aggregates of amphiphilic PS-*b*-PEO diblock copolymers in solution. *Macromolecules* **1998**, *31*, 3509–3518.
- (33) Barreto, J. A.; O'Malley, W.; Kubeil, M.; Graham, B.; Stephan, H.; Spiccia, L. Nanomaterials: Applications in cancer imaging and therapy. *Adv. Mater.* **2011**, *23*, H18–H40.
- (34) Davis, M. E.; Chen, Z. G.; Shin, D. M. Nanoparticle therapeutics: An emerging treatment modality for cancer. *Nat. Rev. Drug Discovery* **2008**, *7*, 771–782.
- (35) Gossman, A.; Okuhata, Y.; Shames, D. M.; Helbich, T. H.; Roberts, T. P. L.; Wendland, M. F.; Huber, S.; Brasch, R. C. Prostate cancer tumor grade differentiation with dynamic contrast-enhanced MR imaging in the rat: Comparison of macromolecular and small-

molecular contrast media - Preliminary experience. *Radiology* **1999**, 213, 265–272.

(36) Su, M. Y.; Mühler, A.; Lao, X.; Nalcioglu, O. Tumor characterization with dynamic contrast-enhanced MRI using MR contrast agents of various molecular weights. *Magn. Reson. Med.* **1998**, 39, 259–269.